JEM Journal of Experimental Medicine

BRIEF DEFINITIVE REPORT

# Amyloidosis of bridging veins is a pathologic feature of Alzheimer's disease

Leon C.D. Smyth[1,2,3,4], Daan Verhaege[1,2], Elio Standen-Bloom[1,2], Yue Wu[5], Yiming Gan[6], Steffen E. Storck[1,2], Pavle Boskovic[1,2], Benjamin A. Plog[1,2], Tornike Mamuladze[1,2], Jose A. Mazzitelli[1,2], Zhuoying Wang[5], Daniel D. Lee[1], Gwendalyn J. Randolph[1], Antoine Drieu[7], Katherine E. Schwetye[1], Song Hu[5], Daniel S. Reich[8], Douglas H. Kelley[6], Rupal I. Mehta[9,10]*, and Jonathan Kipnis[1,2]*

**Alzheimer's disease (AD) is characterized by the accumulation of extracellular aggregated amyloid beta, resulting from impaired waste clearance. We recently identified new cerebrospinal fluid (CSF) efflux structures termed arachnoid cuff exit (ACE) points and speculated that these may be impacted in AD, leading to impaired waste clearance function. Using 5XFAD mice, we found progressive amyloidosis of bridging veins at ACE points. Indeed, in 5XFAD mice, there is impaired CSF efflux to the dura mater, impaired CSF flow along bridging veins, and impaired blood flow through bridging veins. These observations suggest that ACE point amyloidosis plays a role in waste clearance dysfunction in AD. In postmortem human samples, we also found striking amyloidosis of the bridging veins of individuals with AD. Moreover, in human AD specimens, there was prominent bridging vein structural degeneration, indicating advanced pathology and stronger deficits in humans. We propose that bridging vein amyloidosis is an underrecognized pathophysiological correlate of AD that may impair CSF efflux, intracranial pressure, vascular reactivity, and vascular integrity.**

## Introduction

Alzheimer's disease (AD) is characterized by impaired amyloid beta (Aβ) clearance (Mawuenyega et al., 2010). Aβ aggregates multifocally within the brain, including in parenchymal plaques and alongside arteries, causing cerebral amyloid angiopathy (CAA) (Long and Holtzman, 2019; Mehta and Schneider, 2021). The accumulation of Aβ in the brain is thought to be an important trigger for inflammation and tauopathy, which ultimately lead to neuronal loss and cognitive decline (Long and Holtzman, 2019).

Waste clearance in the brain is unique. Whereas most organs contain lymphatic vessels that are specialized in removing wastes and interstitial fluid from the tissue, the central nervous system (CNS) lacks lymphatic vessels. Cerebrospinal fluid (CSF) perfuses the parenchyma, collecting and transporting interstitial waste into the subarachnoid space (Iliff et al., 2012). CSF can then flow along bridging veins, which in turn create discontinuities in the arachnoid barrier, termed arachnoid cuff exit (ACE) points (Smyth et al., 2024). ACE points enable wastes to exit the subarachnoid space, where they can be drained by lymphatic vessels in the dura mater (Smyth et al., 2024). Alongside their role in waste clearance, bridging veins are important for the regulation of cerebral blood flow and intracranial pressure (El Kamouh et al., 2025, *Preprint*).

ACE points are chokepoints in CSF efflux and also contain large smooth muscle-covered bridging veins, suggesting that they could be foci for Aβ accumulation (Smyth et al., 2024). Bridging vein dilation can regulate the exchange of molecules between the dura and the brain, suggesting that changes to the perivascular spaces at ACE points are important in regulating traffic between these two compartments (Mamuladze et al., 2025). Furthermore, there are hints of the accumulation of amyloid in the dura and around bridging veins (Kovacs et al., 2016; Da Mesquita et al., 2021; Rustenhoven et al., 2021; Antila et al., 2024; Plog et al., 2025). Here, we investigated the impact of AD processes on ACE points and defined the consequences for waste clearance and vascular function in AD.

## Results and discussion

ACE points are cuff-like perivascular structures formed around bridging veins exiting the subarachnoid space into the dura

[1]Department of Pathology and Immunology, Washington University School of Medicine, St. Louis, MO, USA; [2]Center for Brain Immunology and Glia (BIG), Washington University School of Medicine, St. Louis, MO, USA; [3]Department of Physiology, Monash University, Clayton, Victoria, Australia; [4]Biomedicine Discovery Institute, Monash University, Clayton, Victoria, Australia; [5]Department of Biomedical Engineering, Danforth Campus, Washington University in St Louis, St. Louis, MO, USA; [6]Department of Mechanical Engineering, University of Rochester, Rochester, NY, USA; [7]Université Paris Cité, Institute of Psychiatry and Neuroscience of Paris (IPNP), INSERM U1266, Paris, France; [8]Translational Neuroradiology Section, National Institute of Neurological Disorders and Stroke, National Institutes of Health, Bethesda, MD, USA; [9]Rush Alzheimer's Disease Center, Rush University Medical Center, Chicago, IL, USA; [10]Department of Pathology, Rush University Medical Center, Chicago, IL, USA.

Correspondence to Leon C.D. Smyth: leon.smyth@monash.edu; Rupal I. Mehta: rupal_mehta@rush.edu; Jonathan Kipnis: kipnis@wustl.edu

*R.I. Mehta and J. Kipnis are co-senior authors.

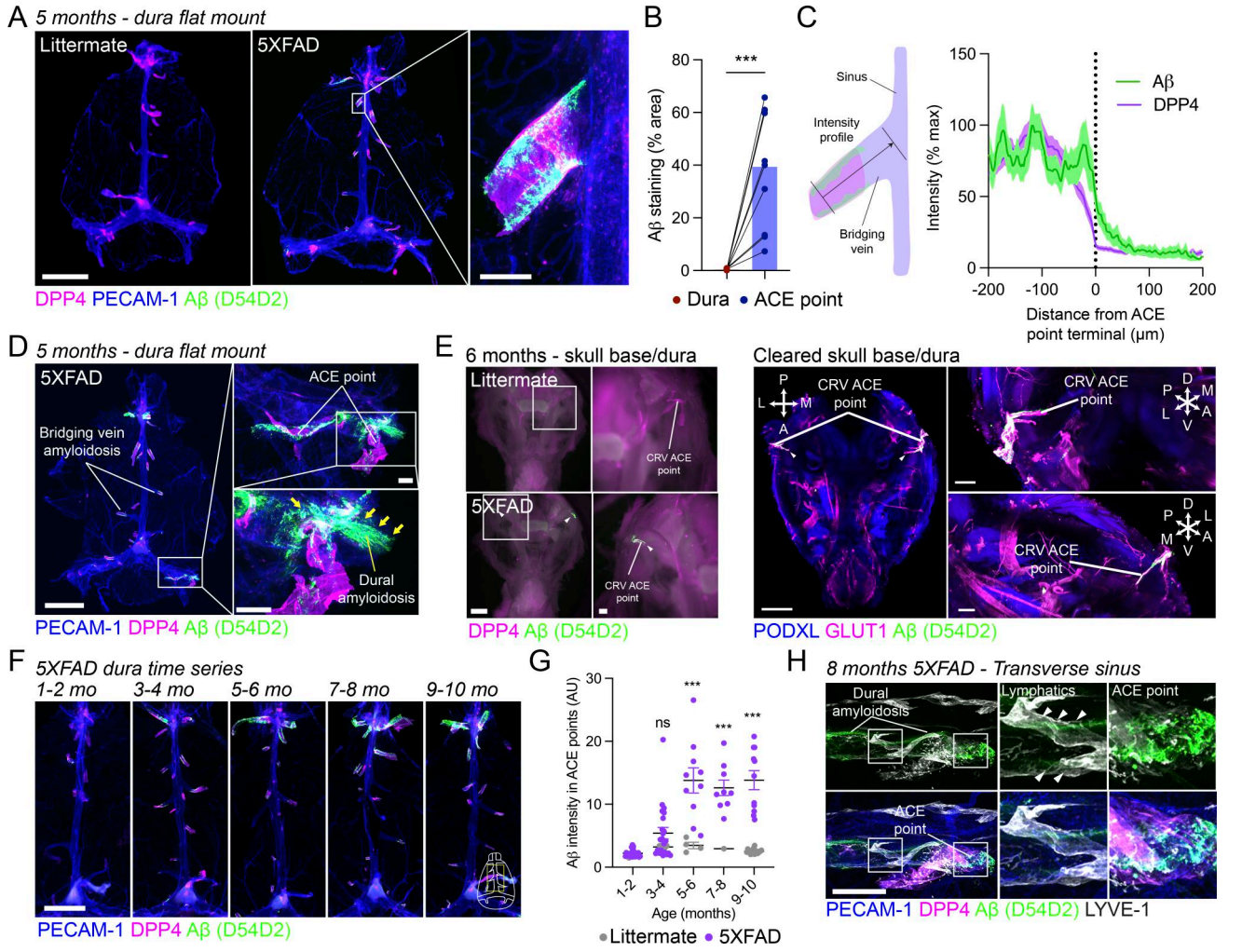


Figure 1. **Progressive amyloidosis of bridging veins in 5XFAD mice. (A)** Representative images of duras from 5-mo-old 5XFAD mice and littermate controls stained for the vascular marker PECAM-1, ACE point marker DPP4, and pan-Aβ antibody D54D2. Scale = 2 mm, inset = 200 µm. **(B)** Quantification of the area of Aβ within ACE points and the rest of the dura in 5XFAD mice. Two-tailed paired *t* test, *N* = 10. ***P < 0.001. **(C)** Schematic for the quantification of Aβ intensity, relative to ACE points. Line profiles of DPP4 and Aβ intensity, relative to the terminal of the ACE point (0 µm). *N* = 44 bridging veins from *N* = 7 5XFAD animals, mean ± SEM. **(D)** Representative image of a 5-mo-old 5XFAD mouse, stained for the vascular marker PECAM-1, ACE point marker DPP4, and pan-Aβ antibody D54D2, highlighting bridging vein and dural amyloidosis. Scale = 2 mm, insets = 200 µm. **(E)** Representative stereomicroscopy images of skull bases (with attached dura) stained with the ACE point marker DPP4 and pan-Aβ antibody D54D2. Representative light-sheet microscopy of a cleared skull base with the vascular marker PODXL, ACE point marker GLUT1, and pan-Aβ antibody D54D2. Scale = 2 mm, insets = 200 µm. **(F)** Representative images of amyloidosis of bridging veins along the superior sagittal sinus of 5XFAD mice up to 10 mo old. Duras are stained for the vascular marker PECAM-1, ACE point marker DPP4, and pan-Aβ antibody D54D2. Scale = 2 mm. **(G)** Quantification of Aβ staining intensity within the DPP4-positive area of ACE points between 1 and 10 mo in 5XFAD mice. Two-way ANOVA with Tukey's post hoc test. Mean ± SEM. P values are given for the comparison between 1- and 2-mo-old 5XFAD and other time points. *N* = 1–22 mice per time point. ns, P > 0.05, nonsignificant; ***P < 0.001. **(H)** Representative images of dural amyloidosis around lymphatic vessels at the transverse sinus. Blood vasculature is stained with PECAM-1, ACE points with DPP4, lymphatic vessels and macrophages with LYVE-1, as well as the pan-Aβ antibody D54D2. Scale = 200 µm.

mater (Smyth et al., 2024). Because ACE points enable CSF efflux to the dura, we aimed to understand whether their function is altered in AD, using the 5XFAD mouse model. We therefore labeled 5XFAD duras with the pan-Aβ antibody D54D2 and the ACE point marker dipeptidylpeptidase-4 (DPP4). We observed striking amyloidosis in 5XFAD duras, confined mainly to bridging veins (Fig. 1, A–C). We speculate that the sharp reduction in amyloidosis around bridging veins as they exited ACE points reflects a transition from the CNS to a compartment containing lymphatic vessels (Da Mesquita et al., 2018; Louveau et al., 2015). In many mice, we also identified amyloid deposition beyond the ACE points around the transverse sinuses (dural amyloidosis) (Fig. 1 D). The presence of Aβ in ACE points in 5XFAD mice confirms the importance of these structures to waste clearance. Indeed, the pattern of amyloidosis along the dorsal dura mater was reminiscent of studies using exogenous tracers (Smyth et al., 2024; Rustenhoven et al., 2021; Louveau et al., 2018). Interestingly, using aggregation-specific dyes, we found that dural amyloidosis around the transverse sinuses was negative for oligothiophene dyes, suggesting that it is less heavily aggregated than bridging vein amyloidosis (Fig. S1 A). Furthermore, solubility fractionation of dural lysates showed

that most amyloid was present in the heavily aggregated formic acid fraction (Fig. S1 B). Recent work has suggested that there is major CSF efflux along the basal cisterns and the basal aspect of the brain (Yoon et al., 2024). Surprisingly, no amyloid deposition was observed on the basal aspect of the dura, ventral to the caudal rhinal vein (Fig. 1 E and Fig. S1, C and D).

We speculated that ACE points may be susceptible to early amyloidosis. We found that bridging vein amyloidosis could be identified in 5XFAD mice as early as 2 mo old, beginning as small aggregates (Fig. 1, F and G). Bridging vein amyloidosis was fully penetrant by 5 mo and was particularly prominent around the rostral rhinal vein (Fig. S1, E and F). Around 5 mo of age, amyloidosis progressed beyond ACE points, with dural amyloidosis beginning to appear around the transverse sinuses, becoming more pronounced until 10 mo (Fig. S1, G and H). Dural amyloidosis was also associated with the extensive lymphatic networks around the transverse sinus (Fig. 1 H). It is possible that lymphatic regression in these regions in 5XFAD mice is a result of direct exposure to amyloid (Da Mesquita et al., 2021).

Interestingly, between 2 and 4 mo, bridging vein amyloidosis was sporadic (Fig. S1 I). Most strikingly, we noted that female animals had consistently higher bridging vein amyloidosis at 3–4 mo of age, likely mirroring stronger parenchymal deposition in female 5XFAD mice (Fig. S1, J and K). Activated microglia compact Aβ plaques in the brain, but less is understood about the interactions of leptomeningeal and perivascular macrophages with vascular plaques (Yuan et al., 2016). Here, we observed the clustering of macrophages to bridging vein amyloidosis, as well as an increase in the expression of lymphatic vessel endothelial hyaluronan receptor 1 (LYVE-1) in macrophages within bridging veins but not the activation marker MHC-II (Fig. S1, L–N). LYVE-1–positive macrophages are highly phagocytic, which may restrict further buildup of amyloid.

We speculated that a consequence of ACE point amyloidosis could be the impaired CSF efflux to the dura. Indeed, we found that tracer efflux to the dura was impaired in 10-mo-old 5XFAD mice (Fig. 2, A and B). Furthermore, particulate tracers could be observed getting stuck in the terminals of ACE points, suggesting amyloid may physically occlude or clog ACE points (Fig. 2 C). We performed particle tracking analysis of CSF flow at ACE points and found that this was also reduced in 5XFAD mice (Fig. 2, D and E). The vasculature is critical to pumping CSF around the subarachnoid space, and CAA is known to impair vascular function, so we speculated that this may play a role in disrupted CSF flow in 5XFAD mice (Kozberg et al., 2025; Holstein-Rønsbo et al., 2023; Mestre et al., 2018). Indeed, we found that the diameter of bridging veins was decreased in 5XFAD mice, as seen in people with AD and possibly reflecting changes in intracranial pressure (Fig. S2, A and B) (El Kamouh et al., 2025, *Preprint*; Pardo et al., 2025). We observed no change in the diameter of perivascular spaces at ACE points, although aggregated amyloid may still restrict available space and increase resistance to CSF efflux (Fig. S2, C and D). To assess structural and functional changes to bridging veins in 5XFAD mice, we performed photoacoustic imaging before and following a hypercapnia challenge that causes vasodilation and increased blood flow to bridging veins (Fig. 2 F) (Cao et al., 2017). As in two-photon microscopy, we observed reduced baseline diameters of bridging veins but also found reduced homeostatic blood flow, suggestive of functional impairment (Fig. 2, G–I). Despite amyloidosis, we saw similar vasodilation in response to hypercapnia, and even stronger increases in blood flow (Fig. 2, J–L). These results suggest that amyloidosis drives functional changes to bridging veins in 5XFAD mice. Although CAA is reported to cause smooth muscle degeneration, we observed no degeneration of vSMCs in 5XFAD bridging veins by 10 mo in the 5XFAD mouse model (Fig. S2, E–G). It is possible that longer exposure to Aβ is required before vSMC loss and dysfunction are observed in this model. We hypothesize that reduced CSF efflux and vascular dysfunction in 5XFAD mice is driven by bridging vein amyloidosis; however, the causal relationship between these phenomena requires further testing.

To investigate if our findings held true in humans, we collected well-preserved postmortem bridging veins from five young adults who were cognitively normal, five older adults without AD pathology who were cognitively normal, and five old adults with AD pathology who exhibited clinical dementia (Fig. 3 A). As in the mouse model, there was striking deposition of Aβ in bridging veins harvested from decedents with AD pathology and dementia (Fig. 3 B and Fig. S3 A). Amyloidosis was almost exclusively formed by $A\beta_{1\text{-}40}$, suggesting a similar composition to CAA found around penetrating and leptomeningeal arteries (Fig. 3 C) (Joachim et al., 1988). Amyloidosis was virtually absent from cognitively normal younger individuals but was found in 3/5 of the cognitively normal older individuals and was present and severe in all cognitively impaired older adults with AD pathology (Fig. 3, D and E). Unlike mice, we observed evidence of severe bridging vein vSMC degeneration in individuals with AD pathology (Fig. S3, B–D), suggesting that vascular function is more strongly impaired in individuals with AD pathology than in 5XFAD mice. It is possible that ACE point dysfunction represents a previously unacknowledged player in CSF dynamics in AD through changes in bridging vein structure and function and associated ACE points (El Kamouh et al., 2025, *Preprint*; Mestre et al., 2018).

Here, we show that ACE points develop severe amyloidosis in 5XFAD mice and humans with AD pathology. Furthermore, CSF efflux and bridging vein function are impaired in 5XFAD mice, suggesting that ACE point dysfunction may be a novel contributor to waste clearance impairment in AD.

The presence of Aβ at ACE points in 5XFAD mice confirms the importance of ACE points to cerebral waste clearance and echoes previous studies using exogenous tracers (Smyth et al., 2024; Rustenhoven et al., 2021; Louveau et al., 2018). It is notable that Aβ aggregation was present at high levels at ACE points along the superior sagittal sinus, in contrast to CSF tracers. We propose that this distribution reflects the different sources (cisterna magna vs. parenchyma), kinetics (bolus vs. extended release), binding, and uptake of the molecules measured. We suggest that ACE points are necessary for CSF efflux to the dura, but that this process is also dependent on efficiency of CSF flow near ACE points and is echoed by strong tracer signals over the olfactory and ambient cisterns, regions of efficient CSF flow that sit underneath bridging veins draining into the rostral rhinal vein and

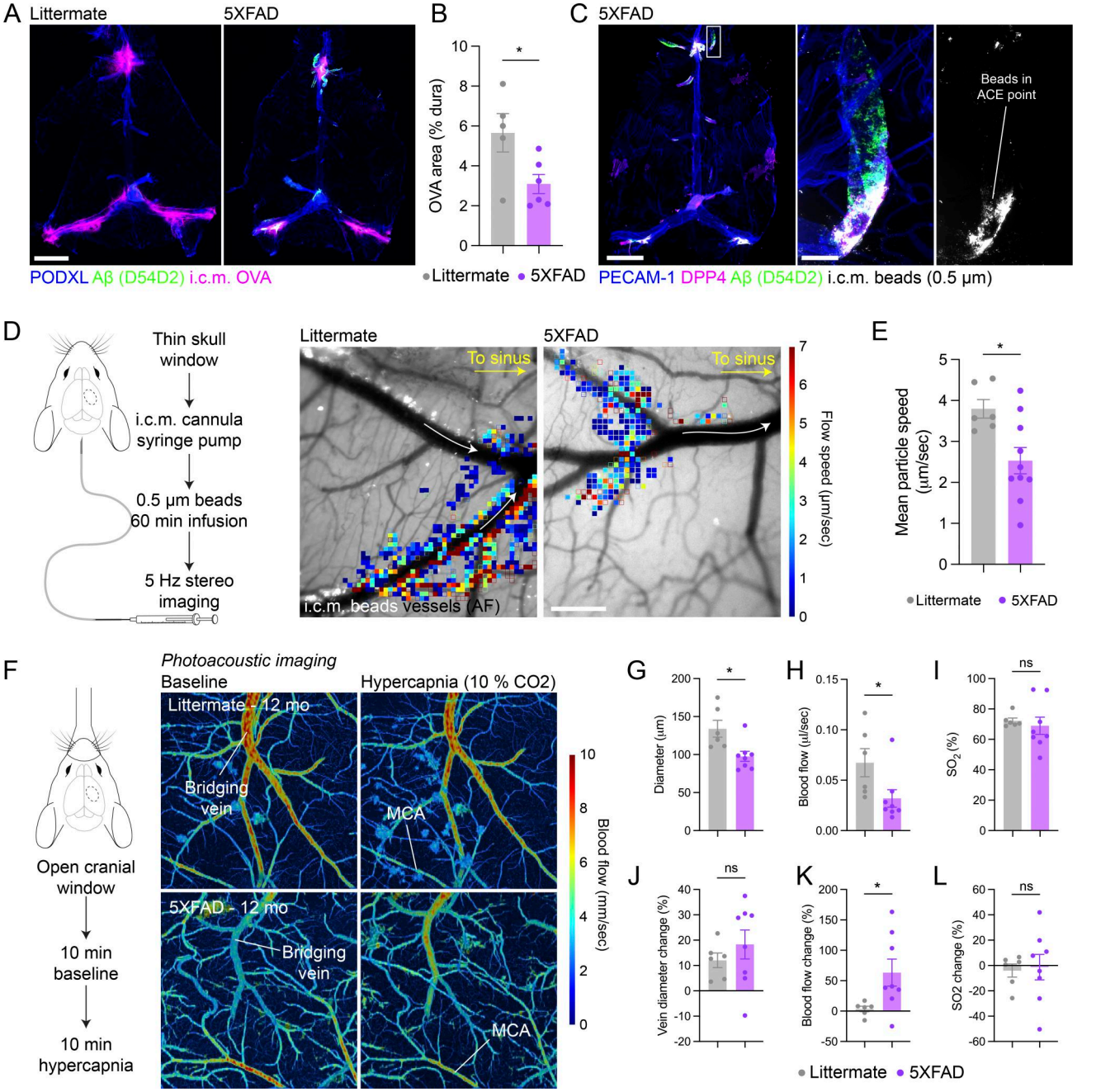


Figure 2. **Disrupted CSF flow and vascular function at ACE points in 5XFAD mice. (A)** Representative images of ICM OVA in the dura of 10-mo-old 5XFAD mice and littermate controls 2 h following injection. Scale = 2 mm. **(B)** Quantification of OVA-positive area in 5XFAD and littermate control duras. Two-tailed unpaired Student's *t* test. *N* = 6 5XFAD, *N* = 5 littermate controls, mean ± SEM. *P < 0.05. **(C)** Representative images of ICM beads trapped within ACE points of a 10-mo-old 5XFAD mouse. Scale = 2 mm, inset = 200 µm. **(D)** Workflow and representative images of particle flow along bridging veins in 8–9-mo-old 5XFAD mice and littermate controls. Scale = 200 µm. **(E)** Quantification of particle flow in 5XFAD and littermate control duras. *N* = 10 5XFAD, *N* = 6 littermate controls. Two-tailed unpaired Student's *t* test, mean ± SEM, *P < 0.05. **(F)** Experimental paradigm and representative images of blood flow speed in leptomeningeal vessels by photoacoustic imaging, colored by blood flow speed. **(G)** Quantification of baseline diameter in 5XFAD and littermate control bridging veins. *N* = 8 5XFAD, *N* = 6 littermate controls. Two-tailed unpaired Student's *t* test, mean ± SEM. *P < 0.05. **(H)** Quantification of baseline blood flow in 5XFAD and littermate control bridging veins. *N* = 8 5XFAD, *N* = 6 littermate controls. Two-tailed unpaired Student's *t* test, mean ± SEM. *P < 0.05. **(I)** Quantification of baseline oxygen saturation ($SO_2$) in 5XFAD and littermate control bridging veins. *N* = 8 5XFAD, *N* = 6 littermate controls. Two-tailed unpaired Student's *t* test, mean ± SEM. ns, P > 0.05, nonsignificant. **(J)** Quantification of the change in diameter in 5XFAD and littermate control bridging veins following hypercapnia. *N* = 8 5XFAD, *N* = 6 littermate controls. Two-tailed unpaired Student's *t* test, mean ± SEM. ns, P > 0.05, nonsignificant. **(K)** Quantification of the change in blood flow in 5XFAD and littermate control bridging veins following hypercapnia. *N* = 8 5XFAD, *N* = 6 littermate controls. Two-tailed unpaired Student's *t* test, mean ± SEM. *P < 0.05. **(L)** Quantification of the change in oxygen saturation in 5XFAD and littermate control bridging veins following hypercapnia. *N* = 8 5XFAD, *N* = 6 littermate controls. Two-tailed unpaired Student's *t* test, mean ± SEM. ns, P > 0.05, nonsignificant.

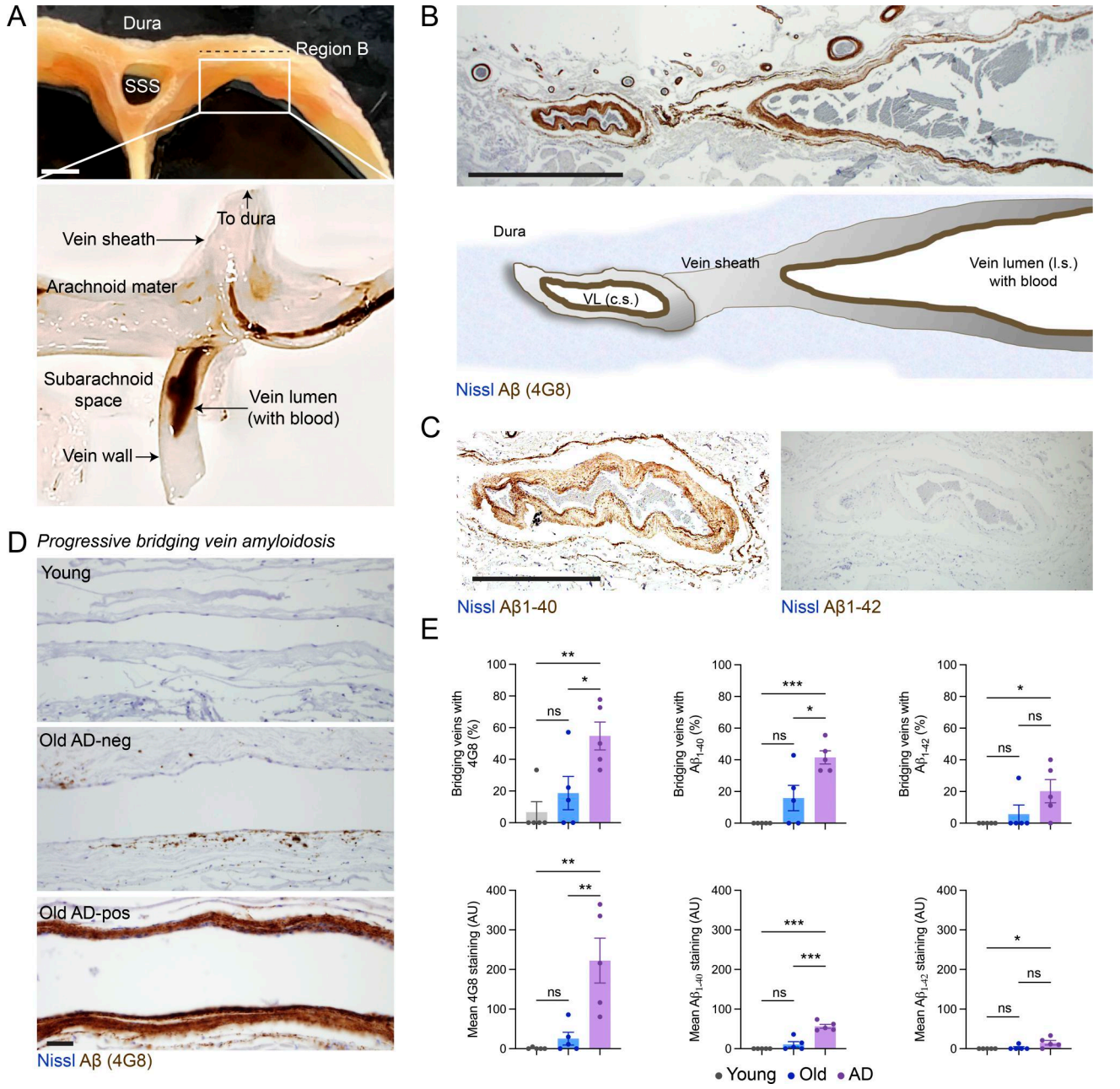


Figure 3. **Amyloidosis of bridging veins in postmortem specimens from cognitively intact adults and cognitively impaired adults with AD pathology and dementia. (A)** Top: Representative low-magnification image of a formalin-fixed paraffin-embedded dural sample, sectioned coronally through the superior sagittal sinus (SSS). Bottom: Representative image of a section through a bridging vein from the dura mater as it drains into the SSS. Scale = 2 mm. **(B)** Representative low-magnification image and schematic of anti–pan-Aβ (4G8) label around a bridging vein in an specimen from an old adult with AD pathology and dementia. Scale = 200 µm. c.s., cross section; l.s., longitudinal section; VL, vein lumen. **(C)** Representative images of anti-$Aβ_{1-40}$ and anti-$Aβ_{1-42}$ labeling around bridging veins from an old adult with AD pathology and dementia. Scale = 200 µm. **(D)** Representative images of anti–pan-Aβ (4G8) labeling in bridging veins from cognitively normal young and old adults without neurological disease and a cognitively impaired adult with AD pathology and dementia. Scale = 200 µm. **(E)** Quantification of the proportion (top row) and intensity (bottom row) of bridging veins stained with anti–pan-Aβ antibody (4G8), and antibodies against anti-$Aβ_{1-40}$ and anti-$Aβ_{1-42}$. *N* = 5. One-way ANOVA with Tukey's post-hoc test, mean ± SEM. *P < 0.05; **P < 0.01; ***P < 0.001; ns, P > 0.05, nonsignificant.

transverse sinus (Chen et al., 2022). On the other hand, the presence of endogenous wastes at ACE points along the superior sagittal sinus indicates that drainage of parenchymal wastes occurs at a slower rate and happens locally, at nearby bridging veins.

We also noted the absence of amyloidosis around ACE points on the basal side of the dura. This was surprising because large volumes of CSF flow along the basal cisterns, and multiple other reports have shown CSF tracer efflux along the basal aspect of the dura (Yoon et al., 2024; Ahn et al., 2019; Ma et al., 2019). It is possible that larger volumes of CSF in the basal cisterns, together with faster rates of CSF flow, may prevent significant Aβ aggregation in this region. Alternatively, CSF in the basal cisterns

may have had less chance to exchange with amyloid-containing brain regions, such as the cerebral cortex and thalamus, in 5XFAD mice. We hypothesize that the accumulation of amyloid around ACE points on the dorsal surface of the brain leads to an increased resistance to CSF flow to the dorsal aspect of the brain and the redistribution of flow along the basal surface that has been observed in CAA models, and reflecting meningeal lymphatic dysfunction (Chen et al., 2022; Gursky et al., 2025; Papadopoulos et al., 2025). Although these results do not challenge the importance of other routes of amyloid clearance in the brain, including the blood–brain barrier (Storck et al., 2016), they reiterate the importance of the dura to amyloid removal (Da Mesquita et al., 2018, 2021).

The accumulation of Aβ along bridging veins, which begins relatively early in 5XFAD mice, suggests that these vessels are particularly susceptible to CAA. This is notable because 5XFAD mice have relatively low levels of CAA, so the presence of bridging vein amyloidosis in 5XFAD mice suggests that it is a particularly robust pathology. The impact of amyloidosis on veins has been largely overlooked due to the low levels of amyloidosis in ascending venules. However, Aβ aggregates have recently been described around veins in animal models of AD, especially in the leptomeninges (Bishay et al., 2022; Klakotskaia et al., 2018; Michaud et al., 2013). Furthermore, amyloidosis of bridging veins has also been observed in APdE9 mice, suggesting that this phenomenon is not unique to the 5XFAD model (Antila et al., 2024).

Very little work has been done on amyloidosis in the dura mater. However, dural amyloidosis has recently come to light as a source of Aβ seeds that can cause iatrogenic CAA (Banerjee et al., 2019; Kovacs et al., 2016). One report found that 13 % of aged subjects had appreciable dural amyloidosis, and published images from this study appear to show deposition around what may be a bridging vein (Kovacs et al., 2016). The human findings of bridging vein amyloidosis were strikingly similar to our observations in 5XFAD mice, with one key exception. The composition of Aβ in human bridging veins was mainly $A\beta_{1\text{-}40}$, while mice mainly had $A\beta_{1\text{-}42}$. This parallels the preponderance of $A\beta_{1\text{-}40}$ in CAA (Joachim et al., 1988; Iwatsubo et al., 1994). We propose that this discrepancy is a function of 5XFAD mice, which overwhelmingly produce $A\beta_{1\text{-}42}$.

We speculated that the deposition of Aβ around bridging veins impacts brain waste clearance through physical obstruction of ACE points and by impacting vascular function. Supporting this notion, we have previously found that physical obstruction of ACE points through bridging vein dilation leads to impaired CSF efflux to the dura (Mamuladze et al., 2025). Here, we found reduced CSF tracer appearing in the dorsal dura. Furthermore, particle speeds at bridging veins in 5XFAD mice were reduced, and particles appeared to become stuck in ACE point termini. On the other hand, amyloidosis leads to vascular stiffening, which can impair vasomotion that drives CSF through the subarachnoid space (Mestre et al., 2018; van Veluw et al., 2020; Holstein-Rønsbo et al., 2023; Kozberg et al., 2025). Furthermore, bridging veins also regulate intracranial pressure and volumes (El Kamouh et al., 2025, *Preprint*). Surprisingly, bridging vein reactivity was preserved in 5XFAD mice, suggesting that bridging veins can still compensate for the accumulation of amyloid in this model through their ability to respond to physiological stimuli. However, reduced diameter and blood flow through bridging veins at baseline suggest that their function is compromised, which may in turn impact intracranial pressure and disrupt CSF flow globally (El Kamouh et al., 2025, *Preprint*). Interestingly, bridging vein walls were highly degenerated in humans with AD pathology. This suggests that vasomotion would be strongly affected in patients or potentially leave bridging veins prone to rupture. Indeed, CAA was recently shown to be associated with subdural hemorrhage, a pathology resulting from the rupture of bridging veins (Rivier et al., 2024). We suggest that bridging vein amyloidosis impairs waste clearance in AD, through its physical obstructive properties as well as its hemodynamic impact (Mawuenyega et al., 2010).

In summary, we found that bridging vein amyloidosis is conserved in mouse models of AD, aged humans, and is prominent in AD subjects. Furthermore, we show that bridging vein amyloidosis is associated with disrupted CSF efflux at ACE points and impaired vascular reactivity of bridging veins in mice. These findings raise many questions and future directions of research. Although we propose that it is likely that ACE point amyloidosis impairs CSF efflux to the dura, we were unable to definitively disentangle the causal relationship. Furthermore, the relative contribution of ACE point occlusion and vascular dysfunction on CSF efflux must also be determined. While the factors that trigger amyloidosis around bridging veins remain unknown, it is possible that macrophage lysosomes seed amyloid deposits in this region, as in the parenchyma (Kaji et al., 2024). Likewise, we speculate that other risk factors, such as apolipoprotein E ε4 genotype, may shift deposition to bridging veins. We propose that perivenous ACE point amyloidosis is an important pathologic feature of AD that could be targeted to improve waste clearance and venous vascular function in AD.

## Materials and methods

### Animals

All mice were housed and bred in a temperature-controlled (22°C) and humidity-controlled (33–39%) environment under a 12 h–12 h light–dark cycle and were provided with food and water ad libitum. No more than five mice were housed together per cage and bred in-house. Heterozygous 5XFAD mice (Tg/+) were bred with littermate controls (+/+) to maintain a heterozygous colony, and heterozygous 5XFAD mice (Tg/+) were compared with wild-type littermate controls (+/+) where genotypes were compared. Both maternal and paternal 5XFAD breeding schemes were used, and the effects of this were not investigated. All mice were used between 2 and 12 mo of age. All experiments and procedures were approved by the Institutional Animal Care and Use Committee at Washington University in St. Louis (23-0145). The following strains were used: 5XFAD (B6.Cg-Tg(APPSwFlLon, PSEN1*M146L*L286V)6799Vas/Mmjax, JAX, 034848), *Dpp4*-CreERT2 (C57BL/6J-*Dpp4*$^{em1(cre/ERT2)Jkpns}$/J, JAX, 039217) (Smyth et al., 2024), and Ai9/LSL-tdTomato (B6.Cg-*Gt(ROSA)26Sor*$^{tm9(CAG\text{-}tdTomato)Hze}$/J, JAX, 007909).

### Mouse dura processing

Mice were euthanized by lethal injection of pentobarbital (euthasol; 10%, vol/vol), followed by transcardiac perfusion of PBS with heparin (20 µ ml$^{-1}$). The mice were then perfusion-fixed with transcardiac perfusion of 10% NBF (Thermo Fisher Scientific). Whole heads were dissected and drop fixed in 10% NBF overnight. Skullcaps were dissected, and duras were peeled from the skullcap and placed in PBS with azide (0.02%, vol/vol) until further use. Before staining, duras were washed twice in PBS and blocked in normal chicken serum in PBS (5%, vol/vol) for 30–60 min. Primary antibodies, diluted in normal donkey serum (1%, vol/vol) in PBS with azide (0.02%, wt/vol) and Triton X-100 (0.2%, vol/vol, Sigma-Aldrich), were added to the duras overnight (details are provided in Table S1). The duras were washed twice in PBS, and secondary antibodies diluted in normal donkey serum (1%, vol/vol) in PBS with azide (0.02%, wt/vol) and Triton X-100 (0.2%, vol/vol; Sigma-Aldrich) were added for 3–4 h at room temperature (details are provided in Table S1). The duras were washed twice in PBS, then placed onto slides and mounted using FluorSave mounting medium (Millipore). Images were acquired by tile scanning on the VS200-S6 slide scanner (Olympus) with a 10× objective (NA 0.4). Final tile scans were stitched together to produce widefield images. Regions of interest were identified, and high-magnification images were acquired using the Stellaris TCS SP8 confocal microscope (Lecia) using either a 20× objective (NA 0.75, Leica) or a 40× objective (NA 1.30, Leica).

### Tissue clearing and light-sheet microscopy

Ventral skulls with dura attached and hemisected skulls with brains removed were decalcified in Morse's solution (10% [wt/vol] sodium citrate [Sigma-Aldrich] and 20% [vol/vol] formic acid [Sigma-Aldrich]) overnight. They were then washed in PBS and stained with antibodies, as above. They were then washed and placed in a refractive index-matching solution (30% [wt/vol] sucrose, 25% [wt/vol] urea, 26% [wt/vol] iohexol, and dissolved in iodixanol; refractive index = 1.50–1.51) overnight (Lee et al., 2025). Samples were then secured in a light-sheet cuvette containing mineral oil (refractive index 1.515). Images were acquired on an UltraMicroscope II (Miltenyi Biotec) light-sheet fluorescence microscope with a 4 µm z-step size. Imaris (Oxford Instruments, v.9.9.1) was used for image processing and visualization.

### Intracisterna magna injections

Mice were anaesthetized with ketamine–xylazine (100 and 10 mg ml$^{-1}$) to achieve a surgical anesthetic plane. The neck was shaved and cleaned with a solution of iodine in 70% (vol/vol) ethanol. The mice were placed in a stereotactic frame, and the skin over the back of the neck was cut. The cisterna magna was exposed by cutting the nuchal muscles. Ovalbumin-AlexaFluor647 conjugate (2.5 µl, 1 mg/ml in artificial CSF; O34781; Thermo Fisher Scientific) was then injected into the cisterna magna with a 5 µl Hamilton syringe with a 33-gauge needle at a rate of ∼2.5 µl min. The needle was then removed, and mice were allowed to recover on a heating pad for 2 h before sacrifice and assessment of the dura mater.

### Intravital imaging of particulate tracers in the CSF

Mice were anaesthetized with ketamine–xylazine (100 and 10 mg ml$^{-1}$) to achieve a surgical anesthetic plane. The neck was shaved and cleaned with a solution of iodine in 70% (vol/vol) ethanol. The mice were placed in a stereotaxic frame, and the scalp was cut. A thin-skull window overlying a dorsal cerebral bridging vein was prepared through careful drilling over an ∼2 mm$^2$ area. Care was taken to use the drill at a slow speed and to avoid thinning the skull too much, as this can damage the arachnoid mater. Mice were then sutured and allowed to recover on a heating pad. Mice were kept for 7–10 days after surgery for further recovery. Mice were then anaesthetized with ketamine–xylazine (100 and 10 mg ml$^{-1}$), and the skin over the back of the neck was shaved. Mice were then prepared for intracisterna magna injection as above. A length of P10 tubing attached to a syringe pump was filled with 0.5-µm fluorescent beads (0.5%, wt/vol; internally dyed yellow-green carboxylate-modified polystyrene spheres; F8813; Thermo Fisher Scientific) was fitted with a 30-G needle tip and gently inserted into the cisterna magna of the mouse. Superglue was placed at the insertion and rapidly cured with a drop of glue accelerator. The scalp was then resected, and a drop of GenTeal Tears gel was placed over the thinned region. Beads were then injected at a rate of 0.25 µl/min for 60 min, and the region was monitored for particle appearance with a fluorescent stereomicroscope (Leica). Once beads had reached the region, particle movement was imaged in the GFP channel, which showed both beads and vessels, at a rate of 5 Hz for 10 min.

### Particle tracking analysis

To measure the speed of CSF flow, we have quantified the motion of the microspheres in each registered time series of images using an automated particle tracking algorithm in MATLAB. This algorithm individually locates each particle with subpixel accuracy, tracks its location throughout the time series of images, and calculates its velocity in each frame. The temporal resolution is ∼4.83 frames per second, and the spatial resolution is ∼1.58 µm per pixel. Each image of the recording has 2,048 × 2,048 pixels. A time series of positions and velocities is obtained for each particle. To ensure that no stagnant particles were included in our measurements, particle tracks with a total displacement lower than a given threshold, typically two pixels, were excluded from the analysis. Particles not located around the perivascular spaces of the vein were excluded by masking. To compute the time-averaged flow velocity and speed, the domain was divided into ∼410 × 410 boxes of resolution 5 × 5 pixels each. All individual velocity measurements for a given time interval were then binned and averaged according to their box positions. Stagnant or nearly stagnant regions were excluded when calculating the changes in flow speed. To evaluate flow speed, we computed the spatial root-mean-square of all speed measurements obtained at each instant of time. To calculate the downstream velocity, we computed the dot product between the time-average flow direction and the instantaneous velocity of the particles of all velocity measurements obtained at each instant of time.

### Tamoxifen-induced recombination

To recombine *Dpp4*-CreER$^{T2}$/LSL-tdTomato mice, tamoxifen (2 mg/day) was injected for five sequential days. Mice were allowed to recover for at least 1 wk prior to imaging.

### Two-photon imaging

Skull thinning in Dpp4-CreER$^{T2}$/LSL-tdTomato mice was performed as above. Mice were allowed to recover for at least 1 wk prior to imaging. Mice were then anaesthetized with ketamine–xylazine (100 and 10 mg ml$^{-1}$), and the scalp was resected. A headplate was glued to the head and placed in a head frame to prevent motion artefact. A drop of saline was placed over the thinned region, and imaging was performed using the A1RHD25 MP microscope (Nikon Instruments) equipped with a resonant scanner. Immediately before scanning, mice were injected retro-orbitally with 0.1 mg of 70-kDa FITC-dextran (90718; Sigma-Aldrich). Z-stack images (2-µm intervals) were acquired using Nikon Elements (v.5.20, Nikon) using the Nikon × 25 water-dipping objective (NA 1.1). A Chameleon Ultra II (Coherent) laser provided excitation at 950 nm.

### Human brain tissues

De-identified postmortem human brain samples (without any linked genetic data) were used in this study. No live humans were included, and IRB was not required. Midfrontal dural samples were harvested from decedents who underwent autopsy within 80 h of death and whose next of kin consented to the use of tissues in research. Medical records were reviewed at the time of autopsy, and for each decedent, the presence and severity of AD neuropathologic change (ADNC) (Montine et al., 2012; Hyman et al., 2012), (co)morbidities, and cause of death were determined by a licensed and board-certified anatomic pathologist with expertise in neuropathology and vascular pathology. A total of 15 dura specimens were obtained from 7 men and 8 women whose age at death ranged from 41 to 84 years (mean, 64.3 years; Table S2). The tissue archive included five brain specimens from persons who were <60 years old at the time of death and 10 brain specimens from persons who were over 60 years old at the time of death. While specimens originated from persons with or without ADNC, those with other detectable neuropathology and/or history of other neurological disease during life were excluded from the study. Bridging veins were identified in variable numbers at the frontal parasagittal vertex of postmortem human brains. On gross (Fig. 2 A) and microscopic (Fig. 2 B) examination, they were observed as large-caliber vessels subjacent to the dural membrane that had relatively large lumens and thin walls and penetrated the dura. The bridging veins were covered by a perivascular sheath. Representative images depicting the anatomy and sampling region are shown in Fig. 2 A. Standard postmortem fixation (i.e., 7–12 days in formalin) was applied, and specimens were paraffin-embedded and then sectioned at 6-µm thickness. Serial sections were deparaffinized and rehydrated through a series of xylenes and ethanol washes and then stained with H&E or processed for immunohistochemistry.

### Immunohistochemistry for human tissue

Deparaffinized rehydrated sections were placed in citrate buffer (10 mM, pH 8.0) and heated at 900 W for 10 min, and then washed in PBS for antigen retrieval. Slides were incubated with a mixture of 5% donkey serum (Sigma-Aldrich) and 0.2% Triton X-100 for 1 h at room temperature before incubation overnight at 4°C with primary antibodies. Subsequently, slides were rinsed again in PBS. Single-label immunohistochemistry was developed using species-specific biotin-conjugated secondary antibody (1:1,000, Vector Laboratories, Burlingame, CA) for 1 h, followed by avidin-biotin peroxidase (Vector Laboratories) for 1h. Sections were then incubated with diaminobenzidine chromogen solution (Thermo Fisher Scientific), and cresyl violet was used as a counterstain to visualize cell nuclei. Chromogen-labeled sections were rinsed, mounted, dehydrated, and coverslipped with DPX mounting medium (Electron Microscopy Services). To better visualize the location of Aβ deposits within veins, double-label immunofluorescence experiments were also performed. For immunofluorescence, deparaffinized, rehydrated sections were incubated overnight with anti-$\beta A_{17\text{-}24}$ antibody (4G8). Subsequently, slides were rinsed and then incubated for 1 h at room temperature with a cocktail of fluorescent-labeled donkey anti-mouse secondary antibody (1:500, Alexa Fluor 488; Invitrogen/Molecular Probes), CY3-conjugated mouse anti-ACTA2 antibody, and 4′,6-diamidino-2-phenylindole (DAPI, Invitrogen). For immunohistochemistry experiments, omission of primary antibody and sections from skin, pancreas, and non-diseased brain were used as negative controls, whereas middle frontal cortical sections originating from individuals with high ADNC were used as positive controls. All sections and controls were immunolabeled as a single batch. Labeled sections were coverslipped with mounting medium. Immunoperoxidase-labeled sections were visualized using an upright brightfield microscope (Olympus BX51; Olympus America, Inc.), and immunofluorescence-labeled sections were visualized using epifluorescence (Nikon Eclipse 90i; Nikon Instruments Inc.) and confocal (Olympus FV3000; Olympus America, Inc.) microscopes.

### Photoacoustic imaging

Following induction with 4% isoflurane in medical air, mice were maintained under 1% isoflurane anesthesia throughout the craniotomy procedure. A longitudinal incision was made to expose the skull, and a 3 × 3 mm$^2$ cranial window was created to allow imaging of the cortical vasculature. After surgery, the mice were sutured and placed in a clean cage to recover. On the same day, mice were anesthetized using a Ketamine/Xylazine cocktail (ketamine: 100 mg/kg; xylazine: 10 mg/kg) and positioned on the animal stage for photoacoustic imaging. The imaging parameters were set as follows: raster scanning mode; laser repetition rate: 6 kHz; laser pulse energy: 100 nJ; field of view: 2 mm × 2 mm; step size: 0.8 µm in the X direction and 10 µm in the Y direction. Then, mice were exposed to a gas mixture containing 10% $CO_2$ in medical air for 10 min, which was followed by a second imaging session. Throughout the imaging process, the body temperature was maintained at ~37°C. Blood oxygen saturation and flow speed were quantified using established

spectral and correlation-based analyses, as described in our previous publication (Cao et al., 2017).

### Image analysis

Images were processed using FIJI (v.2.14.0/1.54 f) and analyzed using CellProfiler (v.4.2.6) or FIJI. For all duras, the pineal gland and third ventricle choroid plexus were digitally removed using FIJI due to autofluorescence. DPP4 was used to guide manual tracing and measurement of intensity within ACE point regions using FIJI to measure the intensity of CD206, LYVE1, and ACTA2. Two-photon measures of bridging vein diameter within and beyond the ACE point (identified by the presence of DPP4-positive cells above the bridging vein) were performed using line profiles in FIJI. Line profiles of amyloid and DPP4 in bridging veins were performed using FIJI. They were aligned to the region where the DPP4 signal dropped to >1500 grey levels, which was approximately the background level. This was classified as the terminal of the ACE point. To define the area of dural amyloidosis, DPP4-positive bridging vein regions were digitally removed using FIJI. CellProfiler was then used to analyze images by thresholding the total dura area, then thresholding Aβ-positive regions to determine the total area of amyloid positivity. Intracisternal tracer coverage was processed similarly, identifying the tracer-positive area as a proportion of the total dural area.

### ELISA for Aβ species

Mouse duras were harvested as described above, omitting fixatives and fixation steps. Duras were then placed in PBS with 2-mm ceramic beads and mechanically homogenized using a bead beater (Bead Mill 4 mini Homogenizer, Thermo Fisher Scientific, 60 s, setting 5). Tubes were spun at 21,000 *g* for 10 min. The supernatant (PBS-soluble fraction) was collected and frozen, and the pellet was resuspended in lysis buffer (2 % (wt/vol) SDS and 1 % (vol/vol) Triton-X100 in PBS). The tissue was homogenized using the bead beater, as above, and spun at 21,000 *g* for 10 min. The supernatant (SDS-soluble fraction) was collected and frozen, the beads were removed, and the pellet was resuspended in formic acid. The tube was agitated using a vortex and kept at room temperature for 10 min before being spun at 21,000 *g* for 10 min. The supernatant was collected (formic acid soluble) and neutralized by the addition of four volumes of neutralization buffer (1 M Tris-base, 0.5 M sodium hydrogen phosphate, and 0.05 % sodium azide). Concentrations of $A\beta_{1\text{-}40}$ and $A\beta_{1\text{-}42}$ were then analyzed using commercially available ELISA kits (KHB3481 [$A\beta_{1\text{-}40}$] and KHB3442 [$A\beta_{1\text{-}42}$], Thermo Fisher Scientific). Absorbance readings (450 nm) were measured using a Synergy H1 (BioTek) plate reader running Gen5 software (v.3.1.1, BioTek). Concentration values were interpolated from an eight-point standard curve (1–0.015 ng $ml^{-1}$ by twofold serial dilution) using linear regression on GraphPad Prism (v.10.4.1).

### Analysis and statistics

Group sizes were not determined using power calculations but, rather, based on similar experiments published by our group. All data are presented as mean ± SEM, including individual values. *N* is representative of the number of animals used, and each point reflects data from an animal. All images shown are representative of at least two independent replications of the original experiment. Data were assumed to be normally distributed, but this was not formally tested. All other data were plotted and analyzed using GraphPad Prism (v.10.4.1). For comparisons involving two groups, an unpaired two-tailed Student's *t* test was performed. For comparisons involving one factor, a one-way ANOVA with Tukey's post hoc test was used. When comparing two factors, two-way ANOVA with Sidak's post hoc test was used.

### Online supplemental material

Fig. S1 shows the aggregation state and spatial distribution of amyloid in the dura, as well as its association with sex and macrophages. Fig. S2 shows changes to the bridging vein and ACE point structure in 5XFAD mice. Fig. S3 shows changes to the bridging veins vessel walls in human specimens. Table S1 lists antibodies and stains. Table S2 lists human subjects.

### Data availability

Data will be made available upon request to the corresponding authors. All relevant code is available in the public domain repository at: https://gitlab-public.circ.rochester.edu/araghuna/bulk-flow-is-not-an-artifact_raghunandan_et_al_2021.git/.

## Acknowledgments

We thank Larysa Kisselbach and Abena Apaw for animal care, Sean Brophy for laboratory management, and all the members of the Kipnis lab for feedback and discussions.

This work was supported by grants from the National Institutes of Health/National Institute on Aging (AG034113 and AG078106 to Jonathan Kipnis; RF1AG083765 and R21AG079221 to Rupal I. Mehta) and the Cure Alzheimer's Fund BEE consortium to Jonathan Kipnis.

Author contributions: Leon C.D. Smyth: conceptualization, data curation, formal analysis, investigation, methodology, project administration, software, supervision, validation, visualization, and writing—original draft, review, and editing. Daan Verhaage: formal analysis, investigation, project administration, and writing—original draft, review, and editing. Elio Standen-Bloom: data curation, formal analysis, investigation, and writing—original draft, review, and editing. Yue Wu: data curation, formal analysis, investigation, methodology, software, and writing—review and editing. Yiming Gan: formal analysis, methodology, software, and visualization. Steffen E. Storck: conceptualization, investigation, and writing—review and editing. Pavle Boskovic: resources and writing—review and editing. Benjamin A. Plog: formal analysis, investigation, writing—review and editing. Tornike Mamuladze: investigation and writing—review and editing. Jose A. Mazzitelli: formal analysis and investigation. Zhuoying Wang: data curation, investigation, methodology, software, and writing—review and editing. Daniel D. Lee: methodology, resources, validation, and writing—review and editing. Gwendalyn J. Randolph: resources, supervision, and writing—review and editing. Antoine Drieu: conceptualization, data curation, investigation, and methodology. Katherine E.

Schwetye: resources. Song Hu: formal analysis, investigation, methodology, and writing—review and editing. Daniel S. Reich: writing—review and editing. Douglas H. Kelley: formal analysis, software, visualization, and writing—review and editing. Rupal I. Mehta: funding acquisition, investigation, methodology, resources, validation, visualization, and writing—original draft, review, and editing. Jonathan Kipnis: conceptualization, funding acquisition, resources, supervision, and writing—original draft, review, and editing.

Disclosures: D.D. Lee reported other from Leinco Technologies Inc. during the conduct of the study; in addition, D.D. Lee had a patent to PCT/US2025/038758 licensed (Leinco Technologies Inc.). G.J. Randolph reported a patent to PCT/US2025/038758 licensed (Leinco Technologies Inc.). D.S. Reich reported grants from Abata Therapeutics and grants from Sanofi outside the submitted work. J. Kipnis is an advisor to IMM, scientific advisory board member of Fibralign, and a co-founder of Rho Bio. No other disclosures were reported.

Submitted: 10 September 2025
Revised: 28 October 2025
Accepted: 29 October 2025

## References

Ahn, J.H., H. Cho, J.-H. Kim, S.H. Kim, J.-S. Ham, I. Park, S.H. Suh, S.P. Hong, J.-H. Song, Y.-K. Hong, et al. 2019. Meningeal lymphatic vessels at the skull base drain cerebrospinal fluid. *Nature*. 572:62–66. https://doi.org/10.1038/s41586-019-1419-5

Antila, S., D. Chilov, H. Nurmi, Z. Li, A. Näsi, M. Gotkiewicz, V. Sitnikova, H. Jäntti, N. Acosta, H. Koivisto, et al. 2024. Sustained meningeal lymphatic vessel atrophy or expansion does not alter Alzheimer's disease-related amyloid pathology. *Nat. Cardiovasc. Res.* 3:474–491. https://doi.org/10.1038/s44161-024-00445-9

Banerjee, G., M.E. Adams, Z. Jaunmuktane, G. Alistair Lammie, B. Turner, M. Wani, I.M.S. Sawhney, H. Houlden, S. Mead, S. Brandner, and D.J. Werring. 2019. Early onset cerebral amyloid angiopathy following childhood exposure to cadaveric dura. *Ann. Neurol.* 85:284–290. https://doi.org/10.1002/ana.25407

Bishay, J., T.L. Beckett, A.Y. Lai, M.E. Hill, D. McMahon, and J. McLaurin. 2022. Venular amyloid accumulation in transgenic Fischer 344 Alzheimer's disease rats. *Sci. Rep.* 12:15287. https://doi.org/10.1038/s41598-022-19549-y

Cao, R., J. Li, B. Ning, N. Sun, T. Wang, Z. Zuo, and S. Hu. 2017. Functional and oxygen-metabolic photoacoustic microscopy of the awake mouse brain. *Neuroimage*. 150:77–87. https://doi.org/10.1016/j.neuroimage.2017.01.049

Chen, X., X. Liu, S. Koundal, R. Elkin, X. Zhu, B. Monte, F. Xu, F. Dai, M. Pedram, H. Lee, et al. 2022. Cerebral amyloid angiopathy is associated with glymphatic transport reduction and time-delayed solute drainage along the neck arteries. *Nat. Aging*. 2:214–223. https://doi.org/10.1038/s43587-022-00181-4

Da Mesquita, S., A. Louveau, A. Vaccari, I. Smirnov, R.C. Cornelison, K.M. Kingsmore, C. Contarino, S. Onengut-Gumuscu, E. Farber, D. Raper, et al. 2018. Functional aspects of meningeal lymphatics in ageing and Alzheimer's disease. *Nature*. 560:185–191. https://doi.org/10.1038/s41586-018-0368-8

Da Mesquita, S., Z. Papadopoulos, T. Dykstra, L. Brase, F.G. Farias, M. Wall, H. Jiang, C.D. Kodira, K.A. de Lima, J. Herz, et al. 2021. Meningeal lymphatics affect microglia responses and anti-Aβ immunotherapy. *Nature*. 593:255–260. https://doi.org/10.1038/s41586-021-03489-0

El Kamouh, M.-R., M. Spajer, R. Singhabahu, K. Sailor, M.-C. Bourrienne, L. Mouton, S. Koundal, D. Doukhi, A. Grine, J. Ninnemann, et al. 2025. Cerebral venous blood flow regulates brain fluid clearance via meningeal lymphatics. *Research Square*. https://doi.org/10.21203/rs.3.rs-5753044/v1 (Preprint posted January 30, 2025).

Gursky, Z., Z.N. Khan, S. Koundal, A. Bhardwaj, J. Caceres Melgarejo, K. Xu, X. Chen, H.-M. Lin, X. Gu, H. Lee, et al. 2025. Age-dependent brain responses to mechanical stress determine resilience in a chronic lymphatic drainage impairment model. *J. Clin. Invest.* 135:e182555. https://doi.org/10.1172/JCI182555

Holstein-Rønsbo, S., Y. Gan, M.J. Giannetto, M.K. Rasmussen, B. Sigurdsson, F.R.M. Beinlich, L. Rose, V. Untiet, L.M. Hablitz, D.H. Kelley, and M. Nedergaard. 2023. Glymphatic influx and clearance are accelerated by neurovascular coupling. *Nat. Neurosci.* 26:1042–1053. https://doi.org/10.1038/s41593-023-01327-2

Hyman, B.T., C.H. Phelps, T.G. Beach, E.H. Bigio, N.J. Cairns, M.C. Carrillo, D.W. Dickson, C. Duyckaerts, M.P. Frosch, E. Masliah, et al. 2012. National Institute on Aging–Alzheimer's Association guidelines for the neuropathologic assessment of Alzheimer's disease. *Alzheimers Dement.* 8:1–13. https://doi.org/10.1016/j.jalz.2011.10.007

Iliff, J.J., M. Wang, Y. Liao, B.A. Plogg, W. Peng, G.A. Gundersen, H. Benveniste, G.E. Vates, R. Deane, S.A. Goldman, et al. 2012. A paravascular pathway facilitates CSF flow through the brain parenchyma and the clearance of interstitial solutes, including amyloid β. *Sci. Transl. Med.* 4:147ra111. https://doi.org/10.1126/scitranslmed.3003748

Iwatsubo, T., A. Odaka, N. Suzuki, H. Mizusawa, N. Nukina, and Y. Ihara. 1994. Visualization of Aβ42(43) and Aβ40 in senile plaques with end-specific Aβ monoclonals: Evidence that an initially deposited species is Aβ42(43). *Neuron*. 13:45–53. https://doi.org/10.1016/0896-6273(94)90458-8

Joachim, C.L., L.K. Duffy, J.H. Morris, and D.J. Selkoe. 1988. Protein chemical and immunocytochemical studies of meningovascular β-amyloid protein in Alzheimer's disease and normal aging. *Brain Res.* 474:100–111. https://doi.org/10.1016/0006-8993(88)90673-7

Kaji, S., S.A. Berghoff, L. Spieth, L. Schlaphoff, A.O. Sasmita, S. Vitale, L. Büschgens, S. Kedia, M. Zirngibl, T. Nazarenko, et al. 2024. Apolipoprotein E aggregation in microglia initiates Alzheimer's disease pathology by seeding β-amyloidosis. *Immunity*. 57:2651–2668.e12. https://doi.org/10.1016/j.immuni.2024.09.014

Klakotskaia, D., C. Agca, R.A. Richardson, E.G. Stopa, T.R. Schachtman, and Y. Agca. 2018. Memory deficiency, cerebral amyloid angiopathy, and amyloid-β plaques in APP+PS1 double transgenic rat model of Alzheimer's disease. *PLoS One*. 13:e0195469. https://doi.org/10.1371/journal.pone.0195469

Kovacs, G.G., M.I. Lutz, G. Ricken, T. Ströbel, R. Höftberger, M. Preusser, G. Regelsberger, S. Hönigschnabl, A. Reiner, P. Fischer, et al. 2016. Dura mater is a potential source of Aβ seeds. *Acta Neuropathol.* 131:911–923. https://doi.org/10.1007/s00401-016-1565-x

Kozberg, M.G., L.P. Munting, L.H. Hanlin, C.A. Auger, M.L. van den Berg, B. Denis de Senneville, L. Hirschler, J.M. Warnking, E.L. Barbier, C.T. Farrar, et al. 2025. Vasomotion loss precedes impaired cerebrovascular reactivity and microbleeds in cerebral amyloid angiopathy. *Brain Commun.* 7:fcaf186. https://doi.org/10.1093/braincomms/fcaf186

Lee, D.D., K.A. Telfer, D.L. Davis, L.C.D. Smyth, R. Ravindran, R.S. Czepielewski, C.G. Huckstep, S. Du, K. Kurashima, A.K. Jain, et al. 2025. ADAPT-3D:accelerated deep adaptable processing of tissue for 3-dimensional fluorescence tissue imaging for research and clinical settings. *Sci. Rep.* 15:31841. https://doi.org/10.1038/s41598-025-16766-z

Long, J.M., and D.M. Holtzman. 2019. Alzheimer disease: An update on pathobiology and treatment strategies. *Cell*. 179:312–339. https://doi.org/10.1016/j.cell.2019.09.001

Louveau, A., J. Herz, M.N. Alme, A.F. Salvador, M.Q. Dong, K.E. Viar, S.G. Herod, J. Knopp, J.C. Setliff, A.L. Lupi, et al. 2018. CNS lymphatic drainage and neuroinflammation are regulated by meningeal lymphatic vasculature. *Nat. Neurosci.* 21:1380–1391. https://doi.org/10.1038/s41593-018-0227-9

Louveau, A., I. Smirnov, T.J. Keyes, J.D. Eccles, S.J. Rouhani, J.D. Peske, N.C. Derecki, D. Castle, J.W. Mandell, K.S. Lee, et al. 2015. Structural and functional features of central nervous system lymphatic vessels. *Nature*. 523:337–341. https://doi.org/10.1038/nature14432

Ma, Q., M. Ries, Y. Decker, A. Müller, C. Riner, A. Bücker, K. Fassbender, M. Detmar, and S.T. Proulx. 2019. Rapid lymphatic efflux limits cerebrospinal fluid flow to the brain. *Acta Neuropathol.* 137:151–165. https://doi.org/10.1007/s00401-018-1916-x

Mamuladze, T., T.H. Zaninelli, L.C.D. Smyth, Y. Wu, D. Abramishvili, R. Silva, B. Imbiakha, D. Verhaege, S. Du, Z. Papadopoulos, et al. 2025. Mast cells regulate the brain-dura interface and CSF dynamics. *Cell*. 188:5487–5498.e16. https://doi.org/10.1016/j.cell.2025.06.046

Mawuenyega, K.G., W. Sigurdson, V. Ovod, L. Munsell, T. Kasten, J.C. Morris, K.E. Yarasheski, and R.J. Bateman. 2010. Decreased clearance of CNS amyloid-β in Alzheimer's disease. *Science*. 330:1774. https://doi.org/10.1126/science.1197623

Mehta, R.I., and J.A. Schneider. 2021. What is 'alzheimer's disease'? The neuropathological heterogeneity of clinically defined Alzheimer's dementia. *Curr. Opin. Neurol.* 34:237–245. https://doi.org/10.1097/WCO.0000000000000912

Mestre, H., J. Tithof, T. Du, W. Song, W. Peng, A.M. Sweeney, G. Olveda, J.H. Thomas, M. Nedergaard, and D.H. Kelley. 2018. Flow of cerebrospinal fluid is driven by arterial pulsations and is reduced in hypertension. *Nat. Commun.* 9:4878. https://doi.org/10.1038/s41467-018-07318-3

Michaud, J.-P., M.-A. Bellavance, P. Préfontaine, and S. Rivest. 2013. Real-time in vivo imaging reveals the ability of monocytes to clear vascular amyloid beta. *Cell Rep.* 5:646–653. https://doi.org/10.1016/j.celrep.2013.10.010

Montine, T.J., C.H. Phelps, T.G. Beach, E.H. Bigio, N.J. Cairns, D.W. Dickson, C. Duyckaerts, M.P. Frosch, E. Masliah, S.S. Mirra, et al. 2012. National Institute on aging–alzheimer's association guidelines for the neuropathologic assessment of Alzheimer's disease: A practical approach. *Acta Neuropathol.* 123:1–11. https://doi.org/10.1007/s00401-011-0910-3

Papadopoulos, Z., L.C.D. Smyth, I. Smirnov, D.A. Gibson, J. Herz, and J. Kipnis. 2025. Differential impact of lymphatic outflow pathways on cerebrospinal fluid homeostasis. *J. Exp. Med.* 222:e20241752. https://doi.org/10.1084/jem.20241752

Pardo, K., V. Khasminsky, O. Keret, F. Benninger, I. Goldberg, I. Shelef, E. Auriel, and A. Glik. 2025. Alzheimer's disease patients have smaller venous drainage system compared to cognitively healthy controls. *Alzheimers Dement.* 21:e14551. https://doi.org/10.1002/alz.14551

Plog, B.A., K. Kim, D. Verhaege, M.W. Kim, Z. Papadopoulos, K. Dikranian, T. Dykstra, J. Cao, R.J. Perrin, K.E. Schwetye, et al. 2025. A route for cerebrospinal fluid flow through leptomeningeal arterial–venous overlaps enables macromolecule and fluid shunting. *Nat. Neurosci.* 28:1436–1445. https://doi.org/10.1038/s41593-025-01977-4

Rivier, C.A., H. Kamel, K.N. Sheth, C. Iadecola, A. Gupta, M.J. de Leon, E. Ross, G.J. Falcone, and S.B. Murthy. 2024. Cerebral amyloid angiopathy and risk of isolated nontraumatic subdural hemorrhage. *JAMA Neurol.* 81:163–169. https://doi.org/10.1001/jamaneurol.2023.4918

Rustenhoven, J., A. Drieu, T. Mamuladze, K.A. de Lima, T. Dykstra, M. Wall, Z. Papadopoulos, M. Kanamori, A.F. Salvador, W. Baker, et al. 2021. Functional characterization of the dural sinuses as a neuroimmune interface. *Cell.* 184:1000–1016.e27. https://doi.org/10.1016/j.cell.2020.12.040

Smyth, L.C.D., D. Xu, S.V. Okar, T. Dykstra, J. Rustenhoven, Z. Papadopoulos, K. Bhasiin, M.W. Kim, A. Drieu, T. Mamuladze, et al. 2024. Identification of direct connections between the dura and the brain. *Nature.* 627:165–173. https://doi.org/10.1038/s41586-023-06993-7

Storck, S.E., S. Meister, J. Nahrath, J.N. Meißner, N. Schubert, A. Di Spiezio, S. Baches, R.E. Vandenbroucke, Y. Bouter, I. Prikulis, et al. 2016. Endothelial LRP1 transports amyloid-$\beta_{1-42}$ across the blood-brain barrier. *J. Clin. Invest.* 126:123–136. https://doi.org/10.1172/JCI81108

van Veluw, S.J., S.S. Hou, M. Calvo-Rodriguez, M. Arbel-Ornath, A.C. Snyder, M.P. Frosch, S.M. Greenberg, and B.J. Bacskai. 2020. Vasomotion as a driving force for paravascular clearance in the awake mouse brain. *Neuron.* 105:549–561.e5. https://doi.org/10.1016/j.neuron.2019.10.033

Yoon, J.-H., H. Jin, H.J. Kim, S.P. Hong, M.J. Yang, J.H. Ahn, Y.-C. Kim, J. Seo, Y. Lee, D.M. McDonald, et al. 2024. Nasopharyngeal lymphatic plexus is a hub for cerebrospinal fluid drainage. *Nature.* 625:768–777. https://doi.org/10.1038/s41586-023-06899-4

Yuan, P., C. Condello, C.D. Keene, Y. Wang, T.D. Bird, S.M. Paul, W. Luo, M. Colonna, D. Baddeley, and J. Grutzendler. 2016. TREM2 haplodeficiency in mice and humans impairs the microglia barrier function leading to decreased amyloid compaction and severe axonal dystrophy. *Neuron.* 90:724–739. https://doi.org/10.1016/j.neuron.2016.05.003

JEM

# Supplemental material

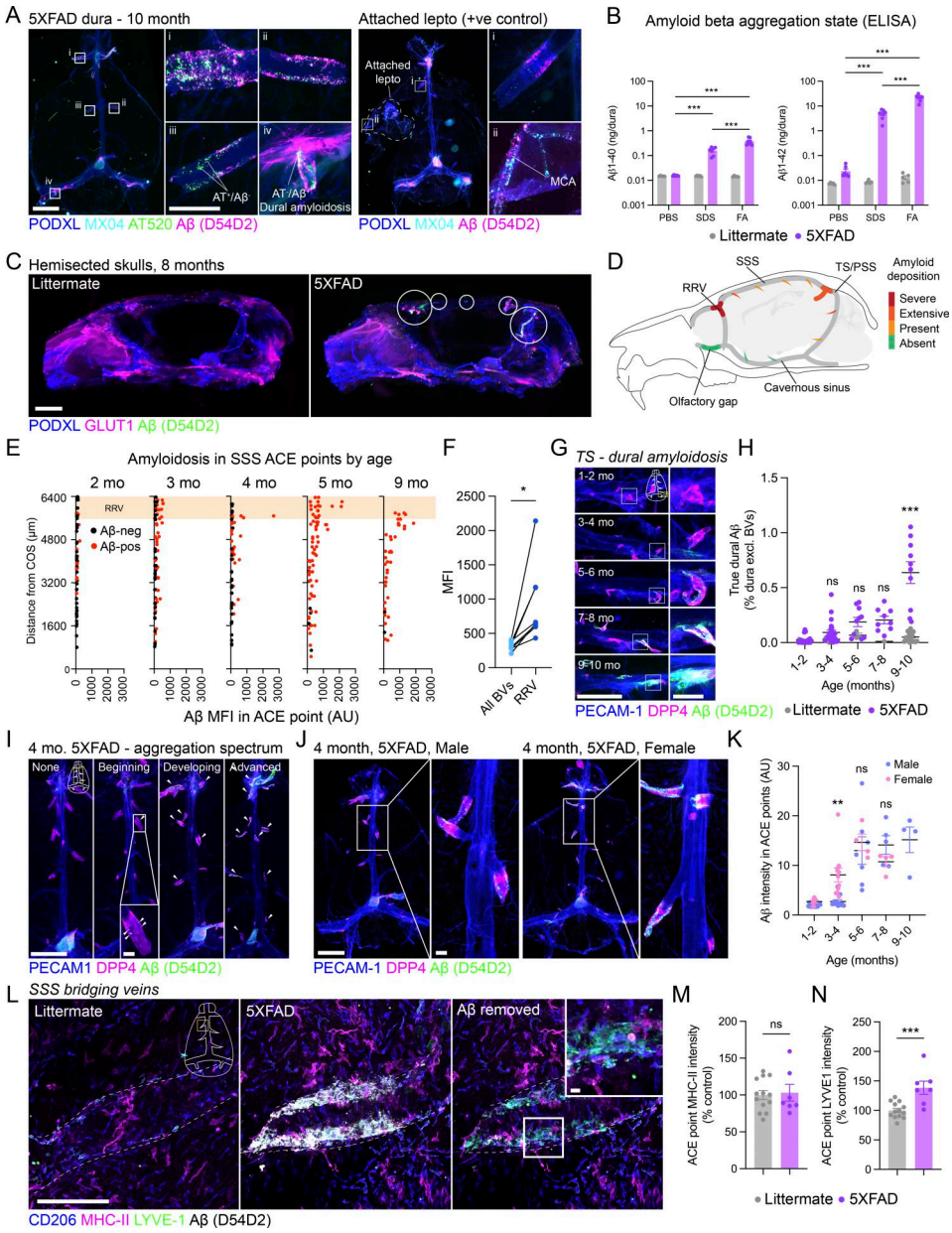


Figure S1. **Aggregation state of Aβ in the dura mater. (A)** Representative images of 10-mo-old 5XFAD duras stained with the aggregated amyloid dye methoxy-X04 (MX04), the oligothiophene AmyTracker520 that binds less aggregated amyloid species, and the pan-Aβ antibody D54D2. A dura containing a fragment of leptomeninges with the middle cerebral artery (MCA) attached is used as a positive control to show positive MX04 staining. Scale = 2 mm, inset = 200 µm. **(B)** Concentrations of differentially soluble species of $A\beta_{1\text{-}40}$ and $A\beta_{1\text{-}42}$ in the dura in 6-mo-old 5XFAD mice. Two-way ANOVA with Tukey's post hoc test, mean ± SEM. Note the log y axis. *N* = 5 littermate controls, 7 5XFAD mice. ***P < 0.001. **(C)** Representative images of cleared hemisected skulls stained for the vascular marker PODXL, ACE point marker GLUT1, and pan-Aβ antibody D54D2. Circled areas reflect regions of amyloidosis. Scale = 2 mm. **(D)** Schematic depicting the relative degree of amyloidosis in ACE points in different regions of the dura mater. **(E)** Quantification of the intensity of Aβ staining in individual bridging veins in 2- to 9-mo-old mice. Veins are classified as either Aβ negative (black) or Aβ positive (red). *N* = 4–8 mice per time point, with 41–86 ACE points quantified per time point. RRV, rostral rhinal vein. **(F)** Quantification of the intensity of Aβ staining in bridging veins draining into the rostral rhinal confluence of sinuses, compared with other bridging veins draining into the superior sagittal sinus. Two-tailed paired *t* test. *N* = 8. *P < 0.05. **(G)** Representative images of amyloid deposition around the transverse sinus, highlighting regions of dural amyloidosis. Scale = 2 mm, inset = 200 µm. **(H)** Quantification of dural amyloidosis area between 1 and 10 mo in 5XFAD mice. Two-way ANOVA with Tukey's post hoc test, mean ± SEM. P values are given for the comparison between 1- and 2-mo-old 5XFAD and other time points. *N* = 1–22 mice per genotype per time point. ns, P > 0.05, nonsignificant; ***P < 0.001. **(I)** Representative images of a spectrum of amyloidosis severity in 4-mo-old 5XFAD mice. Arrowheads depict amyloid-positive bridging veins. Scale = 2 mm, inset = 200 µm. **(J)** Representative images of dura mater from 4-mo-old male and female 5XFAD mice. Scale = 2 mm, inset = 200 µm. **(K)** Quantification of bridging vein amyloidosis in male and female 5XFAD mice. Multiple unpaired *t* tests with Holm-Sidak's adjustment for multiple comparisons, mean ± SEM. *N* = 4–14. ns, P > 0.05, nonsignificant; **P < 0.01. **(L)** Representative images of macrophage markers LYVE-1, CD206, and MHC-II around bridging veins in 5XFAD mice. Scale = 200 µm, inset = 20 µm. **(M)** MHC-II intensity in bridging veins in 5XFAD mice and littermate controls. Two-tailed unpaired Student's *t* test, mean ± SEM. *N* = 13 littermate controls and 7 5XFAD. ns, P > 0.05, nonsignificant. **(N)** LYVE-1 intensity in bridging veins in 5XFAD mice and littermate controls. Two-tailed unpaired Student's *t* test, mean ± SEM. *N* = 3 5XFAD, *N* = 7 littermate controls. ***P < 0.001.

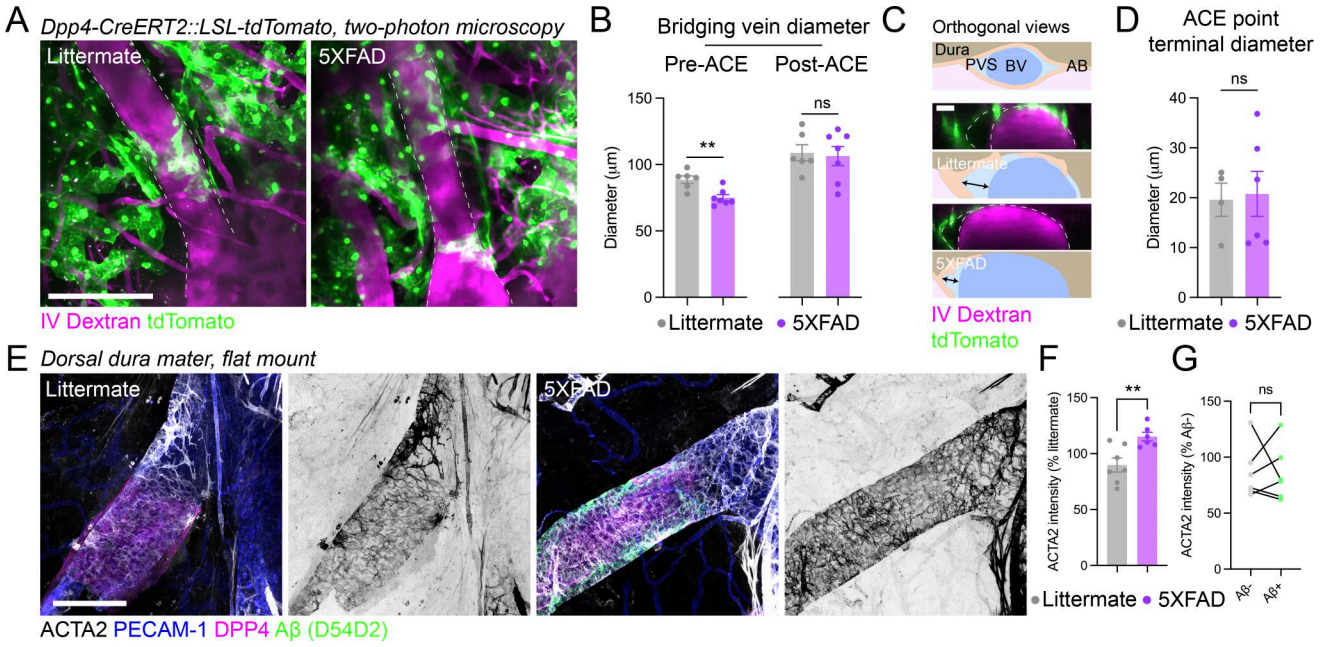


Figure S2. **Altered vascular structure in bridging veins in 5XFAD mice. (A)** Representative maximal z-projections of 5XFAD::Dpp4-CreER$^{T2}$::LSL-tdTomato mice injected (IV) with 70-kDa dextran. Scale = 200 µm. **(B)** Quantification of the diameter of bridging veins within and after the terminal of the ACE point in 5XFAD mice and littermate controls. Two-tailed unpaired Student's *t* tests, mean ± SEM. *N* = 7 5XFAD, *N* = 6 littermate controls. ns, P > 0.05, nonsignificant; **P < 0.01. **(C)** Representative images of ACE point termini and schematic representations in 5XFAD::Dpp4-CreER$^{T2}$::LSL-tdTomato, and littermate controls. Scale = 20 µm. **(D)** Quantification of the terminal diameter of ACE points in 5XFAD::Dpp4-CreER$^{T2}$::LSL-tdTomato mice and littermate controls. Two-tailed unpaired Student's *t* test, mean ± SEM. *N* = 6 5XFAD, *N* = 4 littermate controls. ns, P > 0.05, nonsignificant. **(E)** Representative images of ACTA2-positive venous smooth muscle coverage of bridging veins in 5XFAD mice and littermate controls. Scale = 200 µm. **(F)** Quantification of ACTA2 intensity in bridging veins from littermate controls and 5XFAD mice. Two-tailed unpaired Student's *t* test, mean ± SEM. *N* = 6 5XFAD, *N* = 7 littermate controls. **P < 0.01. **(G)** Quantification of ACTA2 intensity within Aβ-positive and -negative regions of the bridging vein in 5XFAD mice. Two-tailed paired *t* test, *N* = 6. ns, P >0.05, nonsignificant.

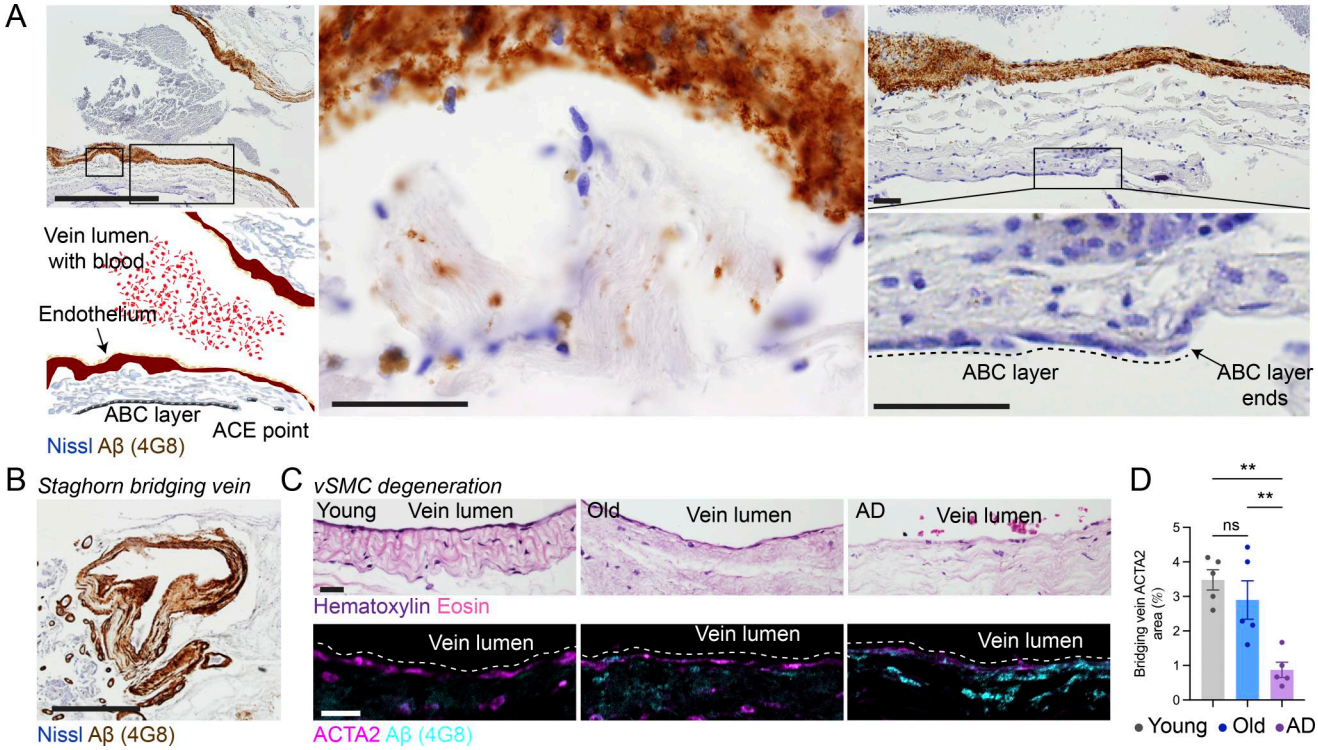


Figure S3. **Bridging vein wall degeneration in AD. (A)** Representative images of amyloidosis in a bridging vein as it passes through an ACE point. Scale = 200 µm, inset = 20 µm. **(B)** Representative images of a staghorn-shaped bridging vein with advanced amyloidosis from a patient with AD. Scale = 200 µm. **(C)** Representative images of H&E and the vascular smooth muscle cell (vSMC) staining for ACTA2 showing bridging vein wall degeneration in AD. Scale = 20 µm. **(D)** Quantification of the area of ACTA2 labeling in bridging veins from young, old, and AD patients. *N* = 5. One-way ANOVA with Tukey's post hoc test, mean ±SEM. ns, P > 0.05, nonsignificant; ** P < 0.01.

**Provided online are Table S1 and Table S2. Table S1 lists antibodies and stains. Table S2 lists human subjects.**